8. TIMING AND CALIBRATIONS FROM THE ATTITUDE RECONSTRUCTION

The attitude reconstruction processes, described in Chapter 7, permitted the calibration of a variety of instrumental and environmental influences acting on the satellite to an accuracy that had not been previously possible. This was a result of the accuracy demanded from, and achieved by, the attitude data, in particular the star mapper transit times combined with the accurate stellar positions provided by the Hipparcos mission. It allowed precise calibration of orientations, scales, drifts and noise levels of gyro readings (used and implemented in the real-time attitude determination), thruster performance (used in the on-ground attitude reconstruction), the detector grid geometry (used in real-time and on-ground attitude reconstruction) and also the inertia tensor (used in on-ground attitude reconstruction). Further analysis of the attitude results also showed what torques were acting on the satellite, and how these torques evolved during the mission. Accurate timing of the measurements was very important for certain aspects of the mission, in particular for minor planet observations and the description of the satellite orbit; the associated calibration procedures are described.

8.1. Characteristics of the Orbit

The satellite described a perturbed elliptical orbit (the geostationary transfer orbit with increased perigee height) with average elements as given in Table 8.1. The decrease rates in semi-major axis and period were directly related to passages through the outer layers of the Earth's atmosphere, and were three to four times higher than the average value when perigee was low, and much smaller when perigee was high. Perigee height varied according to the orientation of the major axis of the orbit with respect to the direction of the Sun as seen from the Earth.

The orbital period had been chosen close to 5 rotational periods of the satellite (38400 s); 9 orbital periods covered close to 4 days. This resulted in semi-periodic patterns of ground-station visibility. In the data processing the successive apogee passages received a monotonically increasing 'orbit number' o (see Volume 1, Section 2.8), helping to relate data reduced by the two reduction consortia for comparison exercises. Successive orbits for which $o_m = \mathrm{mod}(o, 9)$ were equal, were generally very similar in characteristics.

Table 8.1. Characteristics of some of the elements of the satellite orbit: mean value, secular rate of change (unit per year) and amplitude of periodic variations.

Element	Mean value	Change/yr	Amplitude	Unit
period	38340	−20.4	±4.5	s
semi-major axis	24582	−8.2	±2.5	km
eccentricity	0.7196	0.000	±0.005	–
perigee	6890	−3.0	±140	km

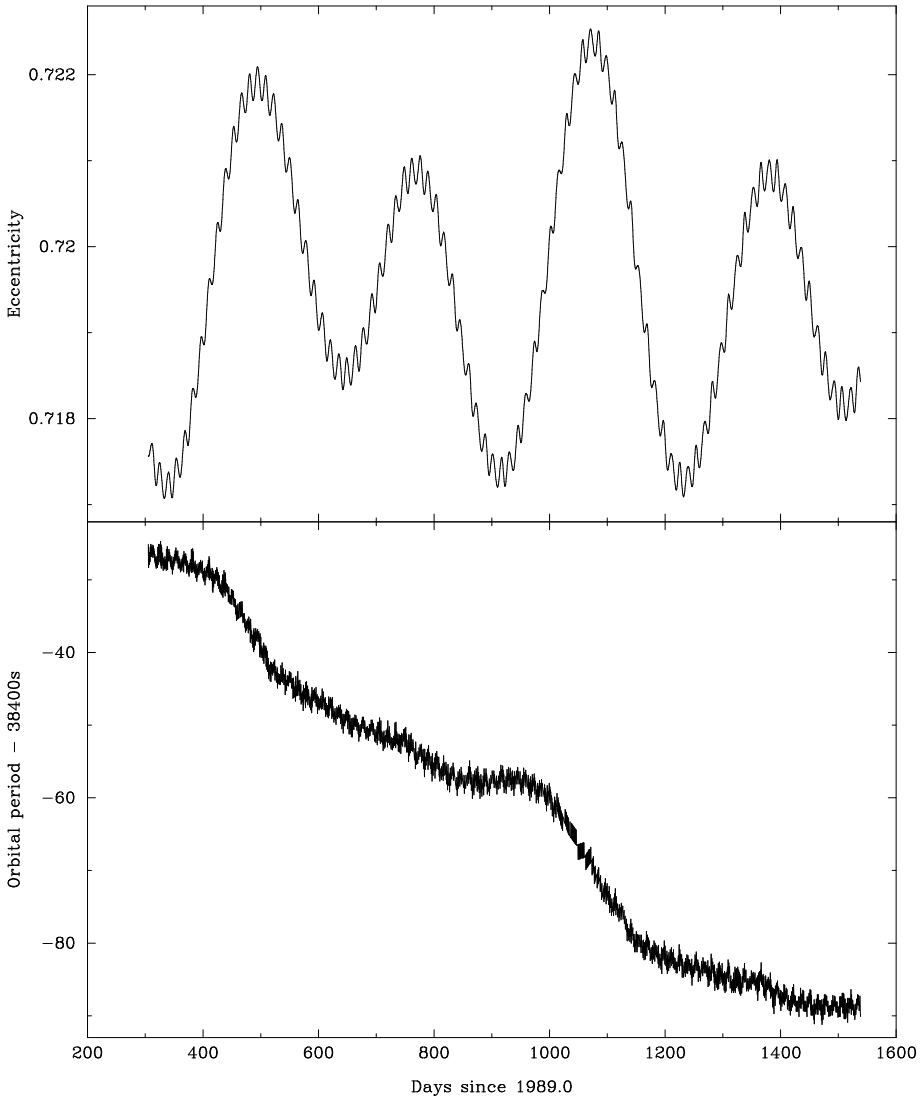

Figure 8.1. *The orbital eccentricity (top) and orbital period (bottom) over the mission. The orbital period is given relative to the intended nominal period for the recovery mission.*

Figure 8.1 shows the evolution of two of the main orbital parameters over the mission. Figure 8.2 shows characteristics of the orbit that directly affected the temperature and other aspects of the satellite: the height, longitude and local time of perigee, reflecting a period of 588.7 days between successive conjunctions of the satellite at apogee and the Sun.

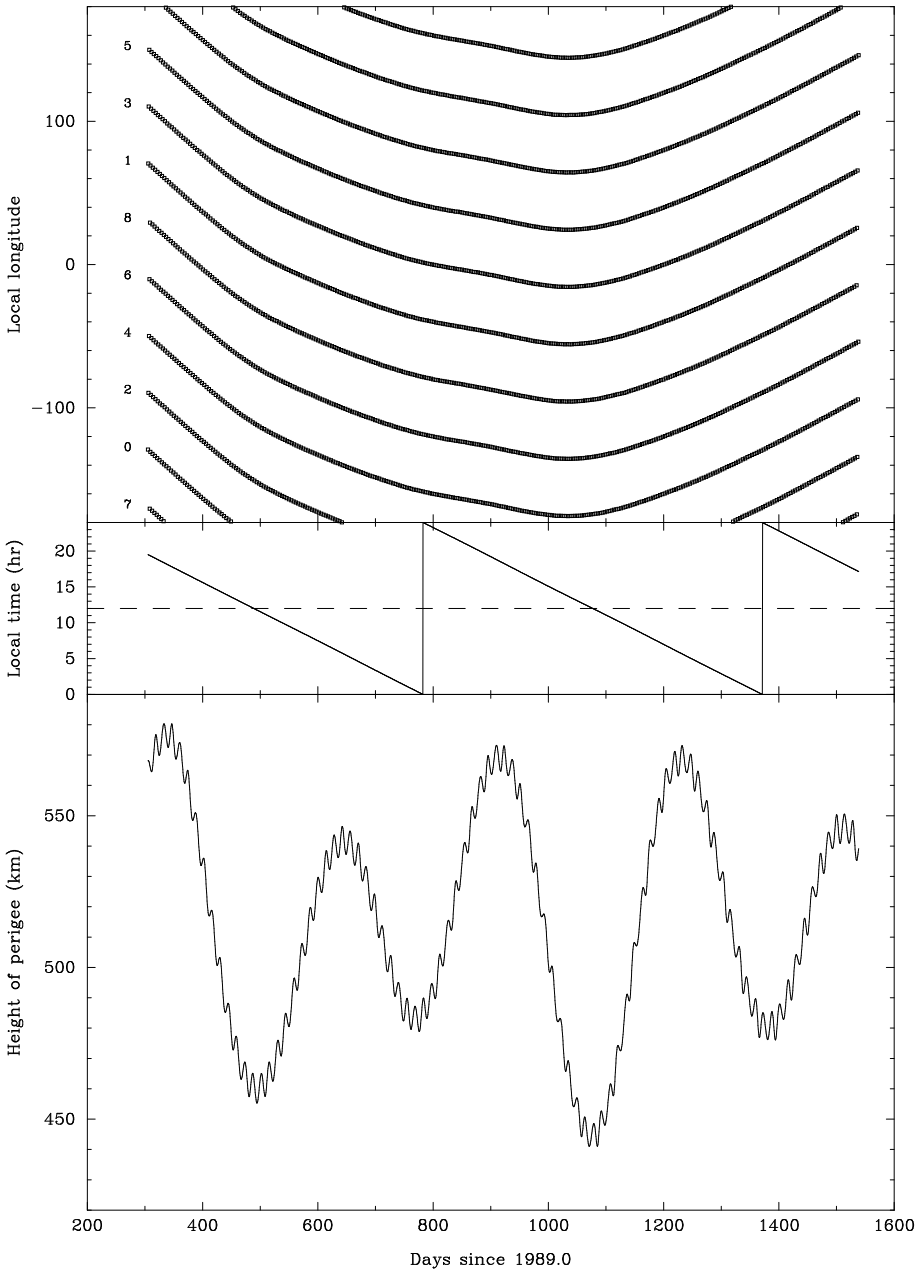

Figure 8.2. *The local geographic longitude for perigee passages (top), the local solar time in hours at perigee (middle) and the perigee height above the Earth's surface (bottom). The numbers in the top graph refer to orbit numbers modulo 9 and show the repeating pattern over 9 orbital periods (4-days) interval. The longitude of apogee falls halfway between successive perigee longitudes. The dashed line in the central graph represents mid-day.*

The local longitude at perigee drifted according to the relation between the orbital period and precession rate of the satellite and the orbital period of the Earth. As the orbital period of the satellite decreased, those drifts changed. Also the precession rate varied according to the orientation of the orbit with respect to the Earth and the Sun. From Figure 8.2 it can be seen that around day 1030 that drift was almost zero. At that time the orbital period was around 38327 s, giving a precession rate for the orbit of $0\overset{\circ}{.}30$ per day, at a time when the perigee passage took place close to mid-day local time. The average precession rate over the mission was $0\overset{\circ}{.}37$ per day.

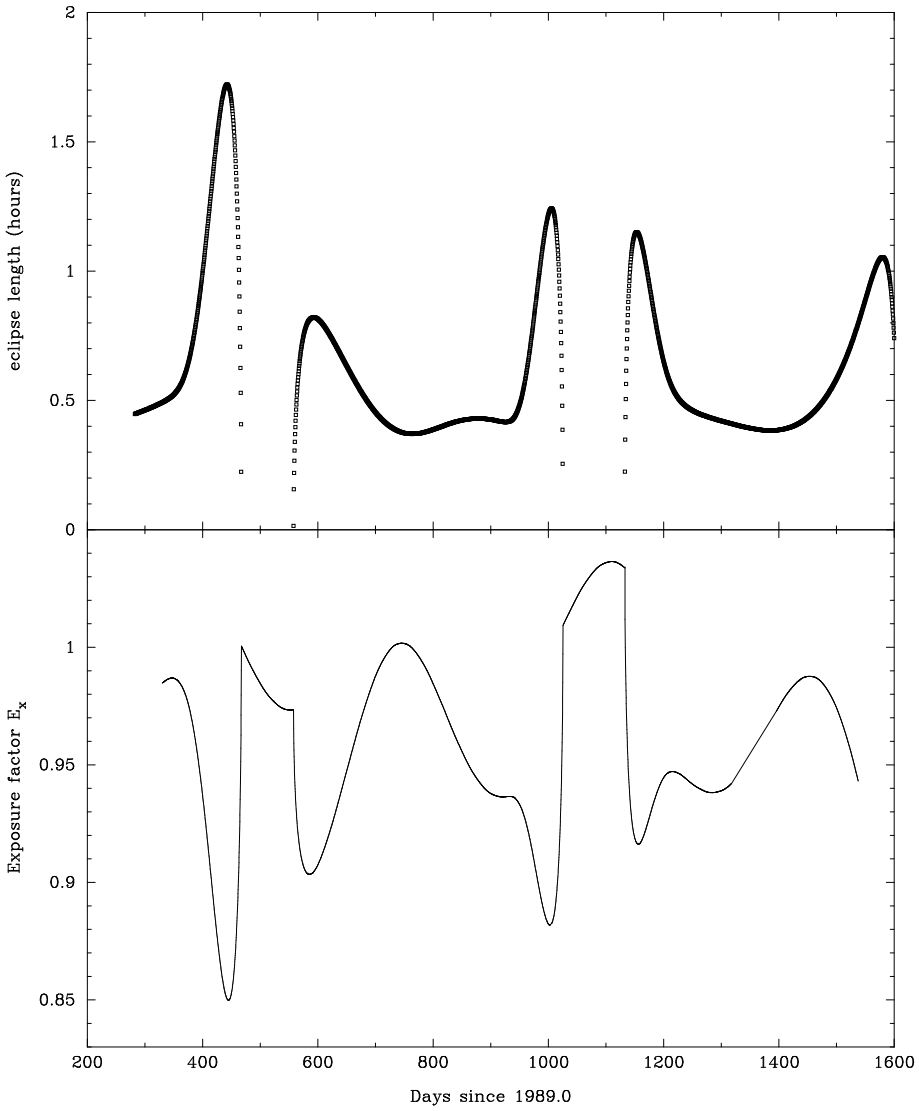

Figure 8.3. *The eclipse lengths (top) and exposure factor (bottom) over the mission.*

As could be expected, the lowest perigee passages took place near mid-day local time, when the satellite orbit was stretched away from the Sun. During these low passages the satellite was subjected to increased friction from the Earth's atmosphere.

In addition to the effects due to the satellite orbit around the Earth, the effects of the Earth's orbit around the Sun were also clearly noticeable. Variations of around ±3.5 per cent in radiation received by the satellite due to the ellipticity of the orbit of the Earth, were reflected in temperature sensitive instrumentation on-board as well as in the solar radiation torques. The radiation received was further affected by the occurrences and lengths of eclipses, shown in Figure 8.3.

To describe the combined effect of eclipses and the solar radiation variations, a quantity E_x, the exposure factor, was introduced and defined as:

$$E_x = \frac{1}{d^2}\left(\frac{T_{\text{orb}} - T_{\text{ecl}}}{T_{\text{orb}}}\right) \qquad [8.1]$$

Table 8.2. The on-board time and the (nominal) time intervals used during the mission. Abbreviations: FOV = field of view, IDT = image dissector tube (main detector), OBT = on-board time, RTAD = real-time attitude determination, SM = star mapper.

Time-span	Frequency	Name	Alias	Use
	921.6 kHz	Oscillator frequency		Basis for all timing
	230.4 kHz	Clock frequency		Input for OBT
0.000833 s	1200 Hz	IDT sampling period	T_1	Integration time for main detector
0.001667 s	600 Hz	SM sampling period		Integration time for SM detectors
0.006667 s	150 Hz	IDT slot	T_2	Allocation of observing time
0.013333 s	75 Hz			Thruster firing time interval unit
0.041667 s	24 Hz	Telemetry frame		Basic unit of telemetry data
0.133333 s	15/2 Hz	IDT interlacing period	T_3	Star switching cycle time
0.416667 s	2.4 Hz			Length of SM extract
1.066667 s	15/16 Hz			Gyro integration time
2.133333 s	15/32 Hz	Observational frame	T_4	IDT observations, RTAD data
10.66667 s	3/32 Hz	Telemetry format		Main unit of telemetry data
20.625 m				Time between crossing of the FOVs
2.1333 h				Rotation period of satellite
10.650 h				Orbital period of satellite

where $T_{\rm orb}$ is the orbital period of the satellite, $T_{\rm ecl}$ the time during an orbit with the Sun eclipsed by the Earth and d the distance between the Earth and the Sun expressed in astronomical units. The variation of E_x, shown in Figure 8.3, was the driving force behind the long-term temperature variations in the spacecraft.

8.2. The On-Board Time

As all the main processing took place using the on-board time as reference, it was necessary to investigate the relations between the on-board and ground-station time. This section deals with the various effects that were observed to influence this relation.

Time Units

All actions on-board the Hipparcos satellite were controlled by timings provided by the on-board time, which derived its signal from a 921.6 kHz crystal controlled oscillator in the bus controller of the central terminal unit, situated on the spacecraft platform almost halfway between the entrance pupils of the two fields of view. Table 8.2 shows the time intervals used, their relationships and the way they were referenced. The basic frequency for the Hipparcos observations was 1200 Hz, equal to the sampling time for the image dissector tube detector (T_1).

The basic frequency for the telemetry was (3/32) Hz, the time of one telemetry format, built up from 256 equal length (24 s^{-1}) telemetry frames. The extraction of star mapper counts was closely related to the telemetry organisation, and the same applied to recordings of thruster firings.

The first stages in the data reductions (star mapper processing, attitude reconstruction, image dissector tube processing, great-circle reduction) were done using the on-board time scales, while carrying along UTC time as provided by the ground stations through time tagging. UTC time was used for the calculation of ephemerides of planets, minor planets and the moons of Jupiter and Saturn and had to be reliable to 0.01 s. It was also used for the calculation of the ephemerides of the satellite, the Earth, Moon and Sun, for determining the barycentric velocity of the satellite and for describing eclipse and occultation conditions.

Satellite to Ground-Station Delays

Delay times between satellite and ground station were calculated from the satellite ephemeris at epoch of observation and the geocentric coordinates of the receiving antenna. These corrections were of the order of 0.01 s to 0.1 s, and were calculated once per telemetry format (see Table 8.2). The calculation involved the following steps:

(1) calculate the Greenwich Mean Sidereal Time (GMST) for the time of observation;

(2) using the GMST and the antenna coordinates, calculate the equatorial station coordinates ($\mathbf{a}$);

(3) using the satellite ephemeris, calculate the geocentric equatorial satellite coordinates ($\mathbf{g}_0$);

(4) calculate the vector $\mathbf{e} = \mathbf{g}_0 - \mathbf{a}$ from the antenna to the satellite;

(5) check if the satellite was above the horizon (observations could continue with the satellite just below the horizon);

(6) calculate the delay time from the length of $\mathbf{e}$;

(7) subtract the delay time from the ground-station time.

The coordinate vectors used for calculating the delay were expressed in the equatorial system of the mean equinox of date, in which the satellite ephemeris was originally provided by ESOC (see Section 12.1). The satellite ephemeris used in the data reductions, e.g. for calculating stellar aberration, was transformed into the J2000 system.

Ground-Station Delay Time Checks

The behaviour of the on-board time was checked with respect to the ground-station time for short (minutes) and long (weeks) time drifts. During these checks it became apparent that ground-station delay times were not as accurate and stable as they were claimed to be, and for some stations were affected by equipment changes. The ground-station delay time described the time interval between the signal reaching the receiver and the moment of tagging the signal. The signal tagging was tuned by using a 1-second block signal from the satellite, to which the ground station had to lock-in. Occasional lock-in errors did occur, causing an error of 1 (and once 2) seconds in the relation between ground-station time and on-board time. These errors were detected from the examination of the evolution of the differences between ground-station and on-board time, and subsequently corrected for. A total of 11 such cases were detected, one from Perth, 4 from Kourou and 6 from Goldstone.

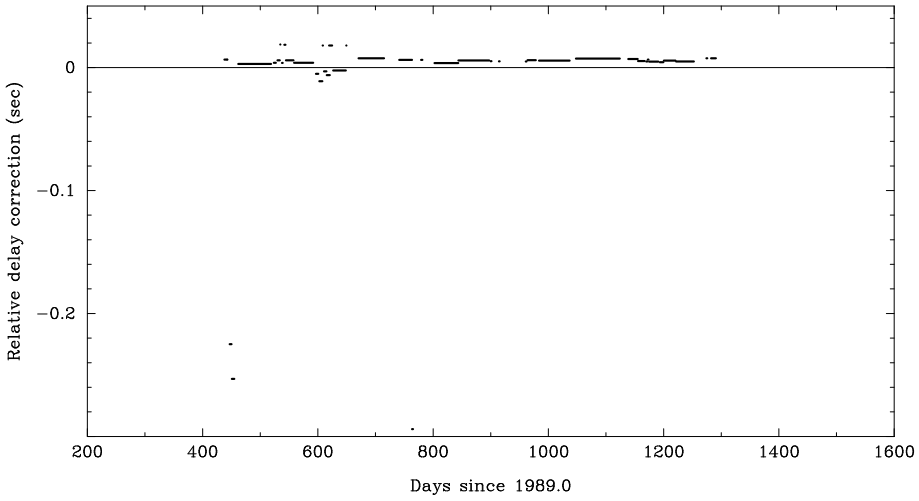

Figure 8.4. *Relative time-delay corrections derived for the Goldstone ground station, excluding the full second corrections.*

The ground-station time delay for the Goldstone receiver was rather unreliable, with sudden changes of several tens of milliseconds, an order of magnitude more than the accuracy that was initially requested. The Goldstone time delays were re-calibrated for the entire mission relative to the much more reliable Odenwald and Perth timings. Ground station change-overs during observations were used for most of these calibrations: the gap in coverage of the observations usually lasted less than a minute. In such a case the relation between on-board time and ground-station time was represented with a simple second-order polynomial over a short stretch covering data before and after the station switch. Two zero points were used in the solution, one for each station. The difference of these zero points was a measure of the relative ground-station delay correction. Comparisons between various determinations showed the most likely source of a correction. Figure 8.4 shows the corrections added by NDAC to the provided Goldstone time delay values (excluding the full second corrections).

On-Board Time Drifts

After adjusting for all the relative ground-station delay corrections, the drift of the on-board time could be determined. This was done by fitting spline functions to the differences between ground-station and on-board time over undisturbed intervals. Almost discrete shifts in these differences occurred when heater problems developed on board the spacecraft, and no solutions could be made across such data. The clock drift was given by the derivative of the spline functions. The drift turned out to consist of two short-time-scale components (the orbital period and the rotation period of the satellite) and a long-time-scale component, related to the orbit of the Earth and the relative position of the satellite orbit with respect to the positions of Sun and Earth. All these effects were caused by temperature changes. Local changes in the case of the rotation period, global changes in the case of the satellite orbit, and longer lasting changes related to the Earth's orbit and the orientation of the satellite orbit with respect to Sun and Earth. Figure 8.5 shows the evolution of the long-term changes, and a comparison with Figure 8.3 identifies beyond reasonable doubt that temperature variations (due to the exposure factor) were the main contributor to the rate variations. The rate variations in Figure 8.5 represent variations of the on-board time at apogee.

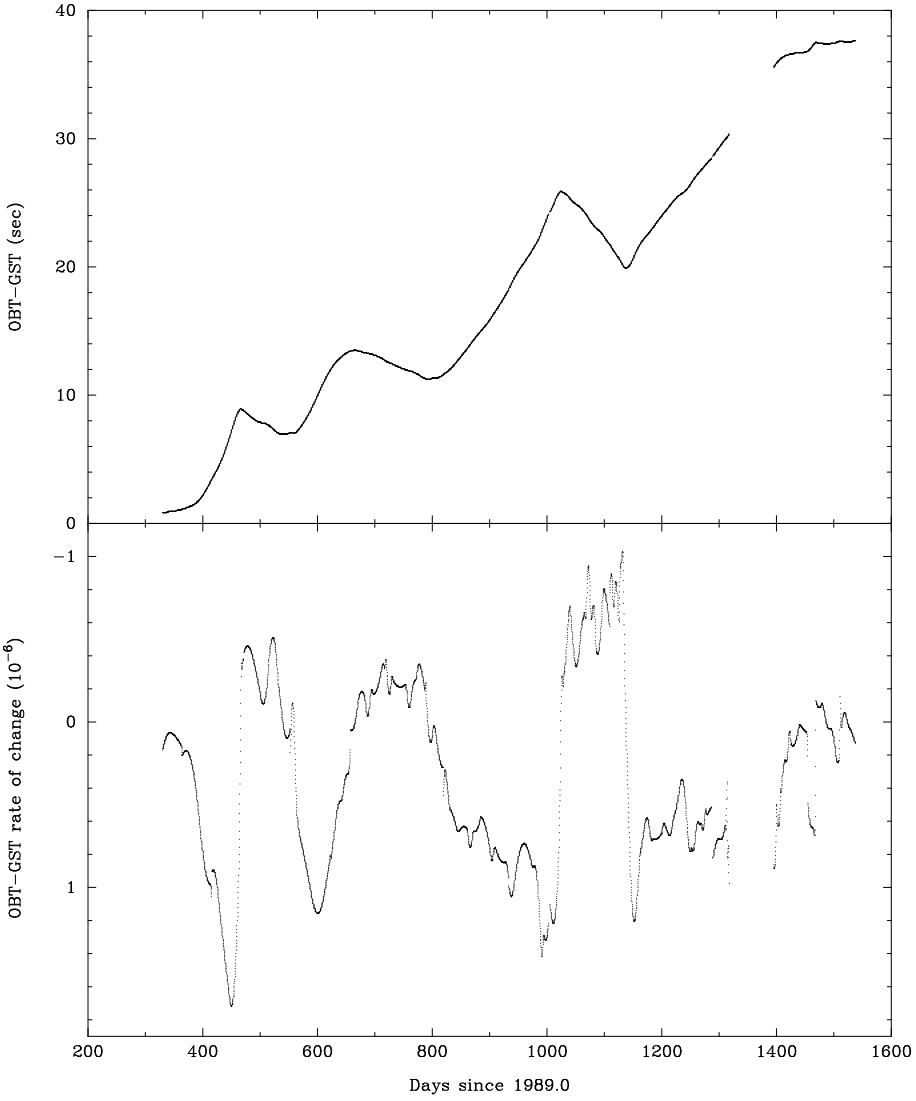

Figure 8.5. *Long-term variations in the on-board time. The top graph shows the measured differences between on-board time (OBT) and ground-station time (GST) over the mission. The bottom graph shows the derivative of the top graph, the rate of change of the time difference OBT–GST, caused by the drift of the on-board time. A comparison between the bottom graph and Figure 8.3 shows that the frequency of the crystal controlled oscillator, which regulated the on-board, increased when the spacecraft cooled down.*

The same relation between on-board time drift and temperature changes can also be seen in Figure 8.6 for the short-term changes, where in this case the spacecraft cools down during eclipses and heats up again outside the eclipses. On top of this variation is a modulation caused by the rotation of the satellite, which causes variations in the local exposure to sunlight. Figure 8.7 shows the effect of heating-up during a perigee passage, and how alternate orbits are more similar in behaviour than consecutive orbits. This is due to the longitudes of the perigee passages as shown in Figure 8.2: for alternate orbits the difference in longitude is much smaller than for consecutive orbits. The density of the Earth's atmosphere at high altitude varies considerably, leading to different amounts of heating up of the spacecraft for perigee passages at different longitudes. This heating up was noticed very clearly when comparing clock drift during periods of low perigee with periods of high perigee.

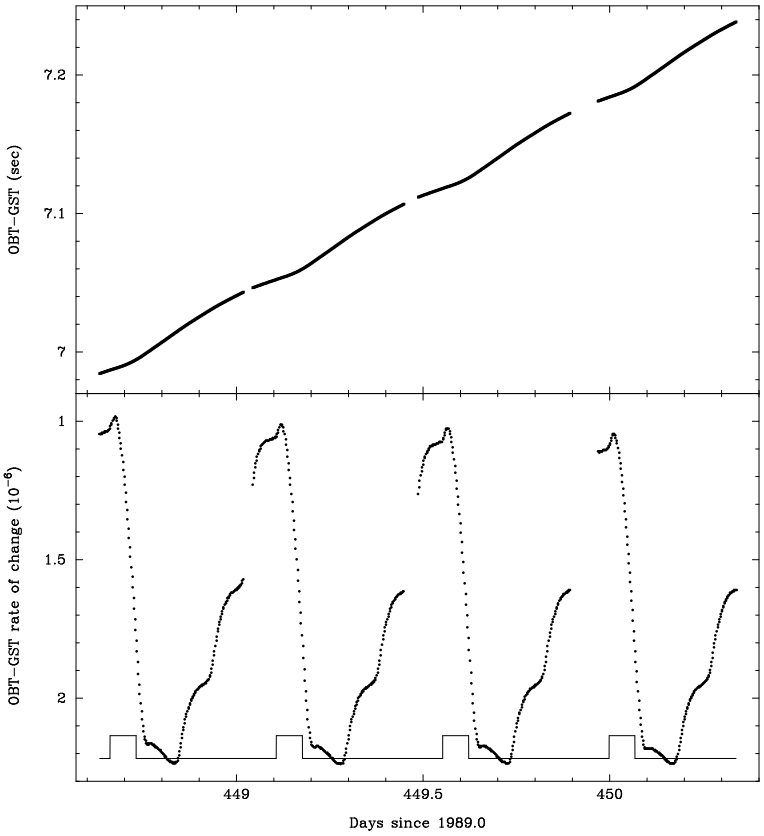

Figure 8.6. *Short-term variations (covering four orbital periods) of the difference between on-board time (OBT) and ground-station time (GST) during a period with long eclipses. The top graph shows the time differences, the lower graph the rate of change in the time difference. The times of eclipses are indicated by the raised sections of the line at the bottom of the lower graph. Cooling down of the spacecraft during eclipses caused the clock to run faster.*

The changes in on-board time drift could be as much as 1×10^{-6} over a period of less than an hour, but was generally at the level of 5×10^{-7} to 2×10^{-7} over one orbit. The maximum drift of the on-board time over one orbit was approximately 0.07 s, which took place when eclipses lasted for almost 90 minutes and the spacecraft cooled down significantly.

FAST derived a third-order polynomial to describe the relation between on-board and ground-station time over one orbit and applied only the full second corrections to the ground-station delay times, while NDAC tagged every observational frame with the corrected ground-station time, corrected for ground-station delay times, determined as described above. The study presented above showed that in both cases sufficient accuracy was obtained for relating the on-board time to Terrestrial Time (TT).

8.3. Gyro Calibrations

The reconstructed attitude provided measurements of the inertial rates of the satellite that could afterwards be compared with the gyro readings for the benefit of the real-time attitude determination and some aspects of the ground-based attitude reconstruction.

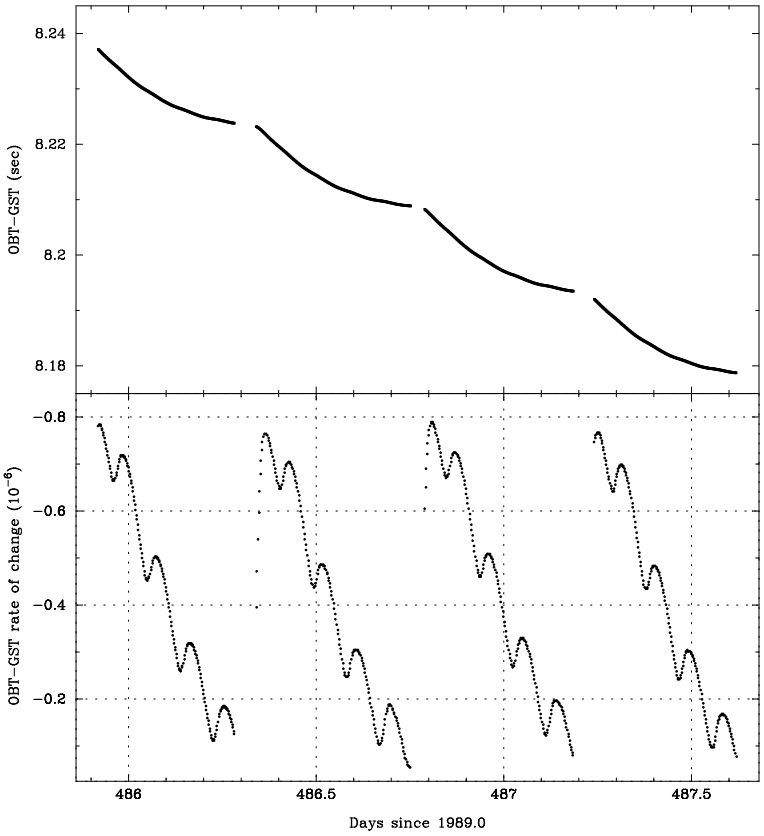

Figure 8.7. *Short-term variations (covering four orbital periods) of the difference between on-board time (OBT) and ground-station time (GST) during a period of low perigee passages. The heating up of the spacecraft during perigee passages, caused the clock to run slower. Details of the variations repeated between alternating orbits, for which the change in local longitude of perigee was relatively small, as shown in Figure 8.2. The 2.13 hour rotation period of the satellite is also clearly seen.*

The comparison described the gyro readings $\mathbf{g}$ as a function of the inertial rates $\boldsymbol{\omega}$ and the gyro drift $\mathbf{g}_d$:

$$\mathbf{g} = \mathbf{A}\boldsymbol{\omega} + \mathbf{g}_d \qquad [8.2]$$

where the matrix $\mathbf{A}$ takes care of the orientation and scaling of the gyro readings. Equation 8.2 was solved for each gyro independently. Noise levels on the various gyros could be very different as well as variable. In order to avoid correlations between the drift and the z axis component of the two gyros in the xy plane, the component ω_z in the solutions for the first two gyros was corrected for the mean scan velocity of the satellite.

Drifts were found to reflect short-term variations due to temperature changes during solar eclipses, and were of the order of 0.1 to 0.4 arcsec s^{-1}. Long-term variations were avoided through the use of thermostatically controlled gyro heaters. Noise levels on the gyro readings were more related to the general deterioration of the gyro electronics over the mission. The evolution of the gyro drifts over the mission is shown in Figure 8.8. The background of the drift variations is unknown. The drifts are given here as measured per gyro, rather than as measured per input axis (as was done in Figure 13.4 in Volume 2).

The gyro readings were made once every 16/15 second (half an observing frame), and were added in pairs, giving one measurement per observing frame. The readout quanta in the operational fine mode were 9×10^{-6} degrees, or 0.03 arcsec per 1.06 s. On a

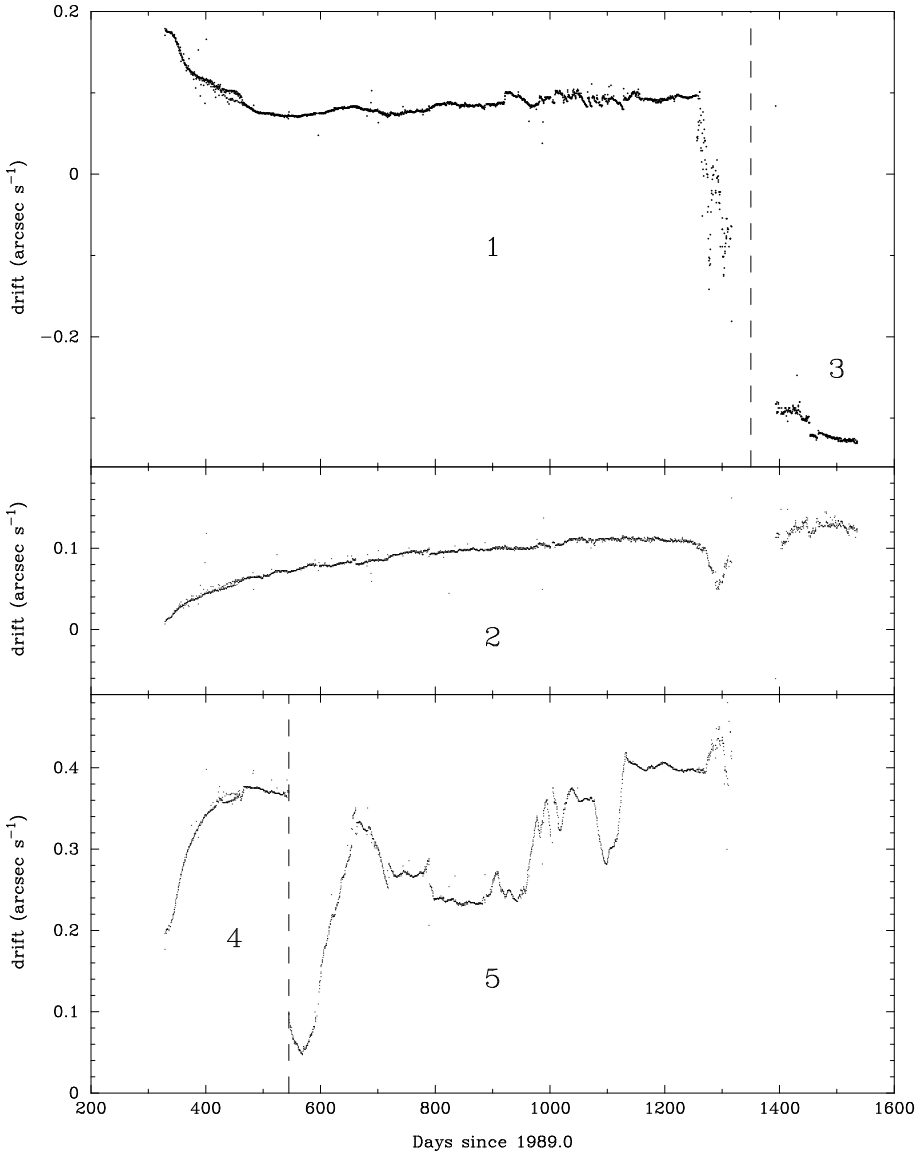

Figure 8.8. *Variations in the drifts of the five gyros (indicated in the graphs by their numbers) over the length of the mission. The noisy region around day 450 is associated with the very long eclipses and large temperature fluctuations around that time. As a result, the measured drift depended on the time coverage of a data set. The discontinuity in the bottom graph around day 545 is due to the change from gyro 4 to gyro 5. For the last part of the mission only two gyros were in operation. The top graph shows the effects of gyro 1 breaking up between day 1260 and day 1320. In the final part of the mission, starting from day 1390, gyro 1 had been replaced by gyro 3, for which the heater had earlier broken down, leading to the relatively large drift and sensitivity to temperature changes in the spacecraft, as shown by the offset around day 1450 to 1460, when the satellite operated in sun-pointing mode.*

single reading this would produce a quantization noise of approximately 0.01 arcsec s^{-1}, and on a pair of measurements a noise of approximately 0.007 arcsec s^{-1}. The standard deviations observed for the gyro readings varied from 0.008 to 0.100 arcsec s^{-1}, with the exception of noise associated with gyro failures. This meant that the quantization noise was in some cases (in particular for gyro 2) a major noise contributor, and that the actual gyro readings in such a case could have been much better. At the noise level

of 0.008 arcsec s^{-1} or less the gyro data could contribute significant information to the attitude reconstruction process, in particular for the z axis position.

Gyro data could obviously only contribute information to the time derivative of the satellite attitude. The contributions of gyro data and the star mapper data to the attitude solution can be estimated from the total data volume W_n for a polynomial coefficient of degree n:

$$W_n = \sum_i \frac{t_i^{2n}}{\langle \epsilon_i^2 \rangle} + \sum_j \frac{n^2 t_j^{2n-2}}{\langle v^2 \rangle}$$

where the first part represents the contribution by the star mapper data and the second part the contribution by the gyro measurements. The variance of the noise on the star mapper transit time determinations is given by $\langle \epsilon_i^2 \rangle$, the variance of the noise on the gyro readings by $\langle v^2 \rangle$. The density of star mapper transits (see Section 6.1) is one every 8 s for the vertical slits, and one every 16 s for the inclined slits in each field of view. The typical error on a transit time was 0.05 arcsec. The possible contribution of gyro data thus depended on the length of the stretch of data considered, the number of star mapper transits available, and the noise level on the gyro readings. The number of star mapper transits available was influenced by density variations on the sky and by background level variations. When gyro noise levels were low (at a level of 0.008 arcsec s^{-1}), gyro data could contribute significant information to the attitude reconstruction process, in particular in situations where the star mapper data was reduced in quantity and/or quality.

The contributions to the standard deviations obtained from the solution of Equation 8.2 consisted of a combination of readout and repositioning noise. Correlations between errors on successive gyro readings were expected and observed, although the exact behaviour was often difficult to understand. The correlation between errors on gyro readings originated from the measuring mechanism: the input axis was to remain 'fixed' with respect to the satellite axes. Thus, a measurement of a rotation angle by a gyro was followed by a resetting of that gyro by the measured angle. It was this resetting that caused the gyro induced torque acting on the spacecraft. Errors on a reading were transmitted to the resetting, and the next reading contained both the error on the resetting and its own error on the reading. In addition, the resetting itself was affected by its own error. As a result of this, consecutive gyro readings had correlated noise, with a correlation coefficient of approximately −0.2. These correlation coefficients could change dramatically with the deterioration of the gyro electronics. When readout noise became dominant, the correlation coefficient could increase to −0.5.

In the case of gyro 3, used over the last 6 months of the mission, the situation was worse. Here, due to a failure of the gyro heater, a wave of amplitude 0.025 arcsec s^{-1} was noticed. The frequency at which it was detected, 0.1488 Hz, could have been an alias of the real frequency with the frequency of observations, 15/32 Hz.

The gyro readings were, especially later in the mission, occasionally disturbed by so–called noise bursts. These were sudden and often dramatic increases in the noise level on the readings of one gyro without an apparent reason. Such changes in noise could not be properly accommodated in the overall calibration of the gyro noise levels, due to their erratic appearance.

During the mission all but one of the gyros broke down, the remaining one operating without a heater. The breaking down of gyro 4 early in the mission was characterised by changes in torques acting on the spacecraft, noticed in the rates measured primarily around the x axis. This could have been caused in two ways: the rotation axis of gyro 4 was changing position significantly, or by changes in the angular momentum of gyro 4. The second of these options seems the more likely one, as it would require rather large

displacement variations of the gyro 4 rotation axis to cause noticeable torque variations. Similar problems were encountered later in the mission when gyro 4 was running in parallel with gyro 5 and at later stages when gyro 5 failed.

The non-operational gyros were tested once every month. A gyro de-storage was not recorded in the telemetry and only the day at which it took place was recorded in the two-weekly operations reports. The examination of the gyro data allowed for an accurate reconstruction of the start of the spin-up, end of spin-up, start of spin-down and end of spin-down times, which were accounted for in two ways: at each of these points an artificial thruster firing was inserted, and the interval between end of spin-up and start of spin-down was recorded in a separate file for use in the torque analysis: while a redundant gyro was running, the torque on the satellite would be quite different. The intervals between start and end of spin-up or spin-down (approximately 1 minute each) were discarded: these intervals were too short with too rapidly changing rates, which made a proper reconstruction of the attitude impossible and modelling not very useful.

8.4. Thruster Firings

The nominal attitude described the planned path of the satellite's z axis on the sky and the associated spin velocity. It was designed so that the scanning of the sky took place in a smooth way, suppressing variations in scanning density across the sky as much as reasonably possible. The satellite was subject to a variety of torques (see Chapter 7), all of which disturbed the pointing and motion of the satellite. Through cold-gas thruster firings the satellite pointing was kept to within 10 arcmin from the nominal attitude.

The firing lengths were calculated on-board the satellite, using a very much simplified model of torques acting on the satellite, the estimated current rotation rates and error angles (real-time attitude determination, see Chapter 7), and the time span over which these error angles were to be brought back to zero. Thruster firings always took place at the start of an observational frame, and lasted an integer number of 1/75 s intervals. At the start of the mission, the minimum time was 0.05 s (4 units) and the maximum time 0.5 s (42 units). Close to perigee longer on-times were allowed. Later in the mission the minimum on-time was reduced to 2/75 s. Initially when one of the error angles was found approaching its limit, all thrusters were fired, later in the mission the z thrusters were only fired if there was the need for at least a minimum length firing of 8/75 s: zero-length z-firings are the most common during that period. A number of times during the mission, due to an update of the Tait-Bryan angles (see Section 7.3) from the ground, the offset between actual and nominal attitude was recognised to be well beyond 10 arcmin. The control software on-board the satellite was not prepared for such a situation, which would have been very rare under nominal conditions. The result of this was a repeated violation of the control condition for the nominal attitude, and minimum length firings of the thrusters in every observational frame (in alternating directions) until the satellite had returned to within the 10 arcmin margin from the nominal attitude. Such data stretches, which could last for several minutes, could not be used in the reductions.

By describing the relation between velocity changes and thruster firing lengths, boundary conditions could be included in the attitude reconstruction software, that allowed for attitude modelling across thruster firings. The relations between thruster firing lengths and velocity changes around the three axes of the satellite were calibrated by means of

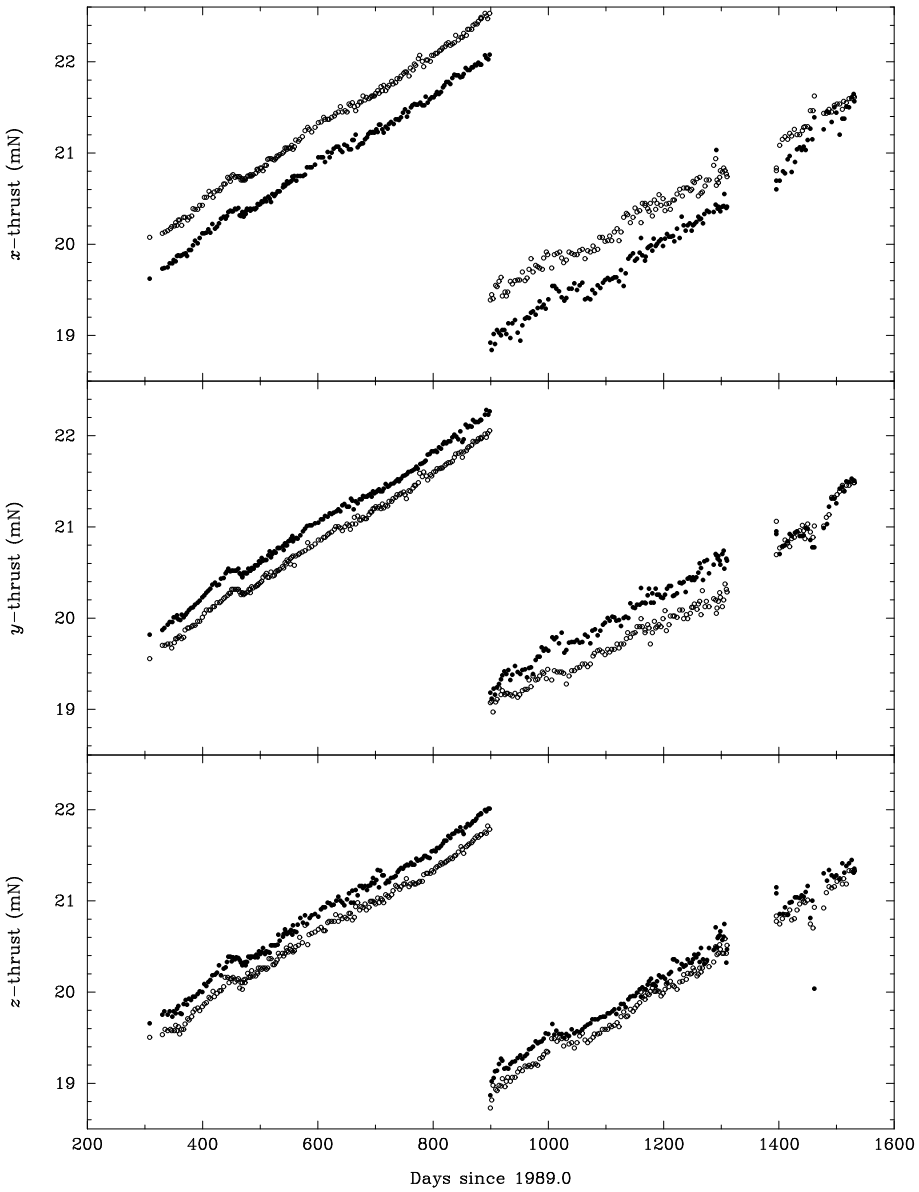

Figure 8.9. *The evolution of the torques produced by the cold-gas thrusters. Thrusters producing positive velocity changes are indicated with filled symbols, those producing negative changes with open symbols. The discontinuity is due to a change of gas tank, the drift is due to the emptying of the gas tanks and a slight over-compensation for loss of pressure.*

on average two days of data. Using the reconstructed attitude the changes in velocity on all three axes across a thruster firing were measured. Separate calibrations were made for thrusters causing positive velocity changes and for thrusters causing negative velocity changes, 6 components in all. In a least-squares solution these changes were expressed as linear functions of the recorded on-times of the thrusters and an offset. Table 8.3 shows for each thruster the measured offsets, expressed as zero points in the on-time. Slow increases in the zero-point values were observed, as well as some increase coinciding with the gas-tank change-over. In general, the zero points were stable to within 5 per cent of 1/75 s.

Table 8.3. The zero points in the thruster on-times, given in units of 1/75 s.

Axis	+Thrust	−Thrust
x	0.65	0.90
y	0.70	0.90
z	0.60	0.70

The linear relation between the change in rotation rate dv and the thrust t activated over an interval τ describes the acceleration caused by the thruster involved, which, using the arm-length of the thruster and the inertia tensor of the satellite, can be translated into a torque. Figure 8.9 shows the evolution of the torques produced by the 6 thrusters over the mission. The sudden change at day 900 is due to a change of gas tank. The increase in torque over the mission is due to depletion of the gas tanks, with the decreasing pressure being over-compensated. Further modulations were related to temperature variations of the spacecraft. This is most notably so for the peak around day 450, which is related to the minimum in the exposure factor shown in Figure 8.3: with the spacecraft cooled down, the pressure in the gas tanks was diminished, and automatically over-compensated to give a higher resulting torque. The thruster torque specified by the manufacturer was 20 mN.

In the nominal situation (geostationary orbit, empty apogee boost motor tank) the mass centre of the satellite would have coincided with the plane in which the z thrusters were situated. However, with a full tank the mass centre was shifted by 72 cm, which resulted in the z thrusters also causing torques on the x and y axes. The calibration values obtained for the z thrusters confirmed the estimate of the mass centre of the satellite by the manufacturer to within a few mm. Figure 8.10 shows the x and y components in the z thrusters as calibrated in comparison with the values predicted from the positions of the thrusters and the mass centre.

The noise level left after fitting the thruster firing lengths against the changes in rotation rates was an indication of the precision to which this information could be used in the reductions. The figures observed changed significantly from 0.01 arcsec s^{-1} for the first gas tank to 0.02 arcsec s^{-1} for the second tank. That means that after a thruster firing the uncertainty in the rotation rates is at least at a level of 0.01 to 0.02 arcsec s^{-1}, and at most at the level of 0.1 arcsec s^{-1}. The noise was independent of firing length. The increase in the noise level while using the second gas tank could be due to stronger temperature fluctuations resulting from a different position in the spacecraft.

8.5. Inertia Tensor and Torque Calibrations

Basic Model

The calibration of the inertia tensor and of the environmental torques relied on the fact that the attitude reconstruction results were available for all three axes in the form of rates, and when differentiated, in the form of accelerations. If we assume that the

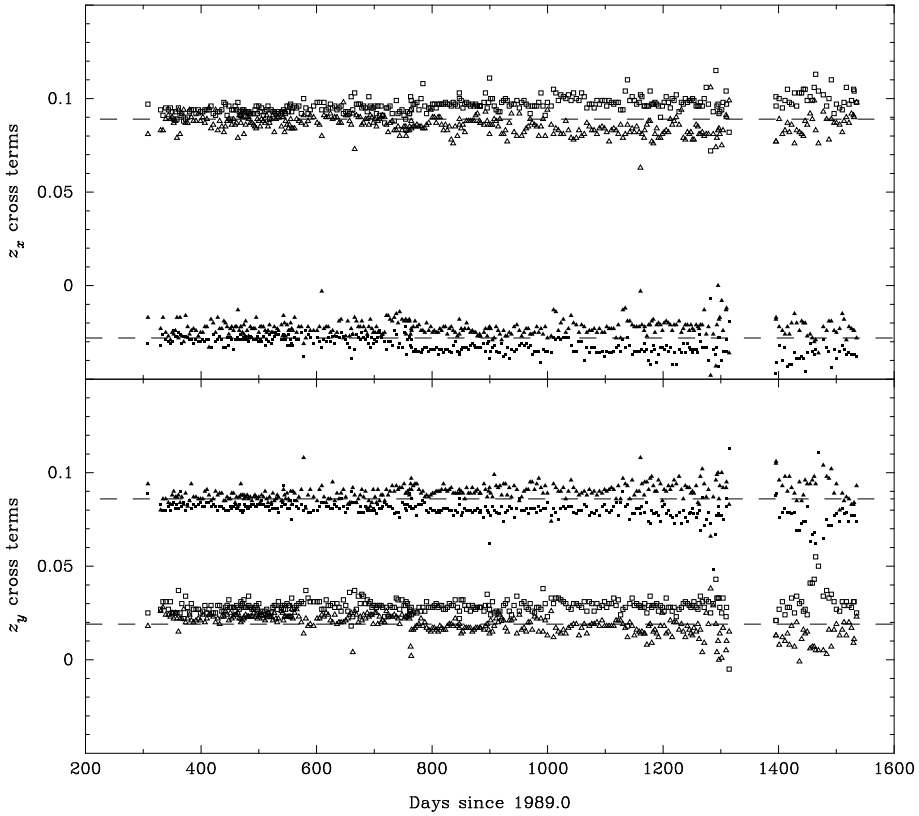

Figure 8.10. *The relative torques caused by the z thrusters on the x and y rotation rates. Nominally, a firing by the +z thruster, giving a velocity change of v_z, also gave a velocity change of $-0.028\ v_z$ on the x axis, and $+0.086\ v_z$ on the y axis (solid symbols). Similarly, a firing by the −z thruster, giving a velocity change of $-v_z$, also gave a velocity change of $-0.089\ v_z$ on the x- and $-0.019\ v_z$ on the y axis (open symbols).*

Hipparcos satellite was a rigid body moving freely in space, then the relation between the rates and the accelerations was described by the Euler equation:

$$\mathbf{I}\,\frac{\mathrm{d}\boldsymbol{\omega}}{\mathrm{d}t} = \mathbf{N} - \boldsymbol{\omega} \times \mathbf{I}\,\boldsymbol{\omega} \qquad [8.3]$$

where **I** is the inertia tensor, **N** the external torques and $\boldsymbol{\omega}$ the inertial rates around the satellite axes. Thus, $\boldsymbol{\omega}$ and $\mathrm{d}\boldsymbol{\omega}/\mathrm{d}t$ were observed, and **N** and **I** were to be calibrated. In principle one should first orthogonalize the left-hand side of Equation 8.3, but using the ground-based starting values of the inertia tensor, this orthogonalization would have very little effect (considering also that the magnitudes of the acceleration rates for the three axes are not very different). Thus, it was assumed that in a first approximation the left-hand side of Equation 8.3 could be expressed as:

$$\mathbf{I}\,\frac{\mathrm{d}\boldsymbol{\omega}}{\mathrm{d}t} = \begin{pmatrix} I_{xx}\dot{\omega}_x \\ I_{yy}\dot{\omega}_y \\ I_{zz}\dot{\omega}_z \end{pmatrix} \qquad [8.4]$$

where I_{xx}, I_{yy} and I_{zz} are the diagonal elements of the inertia tensor. The off-diagonal elements of **I** were approximately 100 times smaller than the diagonal elements (see Table 7.1). Small changes in the inertia tensor elements were most likely related to the depletion of the cold-gas tanks.

The same approximation could not be made for the second term on the right-hand side of Equation 8.3. Developing this term for the x coordinate gives:

$$\left[\boldsymbol{\omega} \times \mathbf{I}\,\boldsymbol{\omega}\right]_x = \omega_y\omega_z(I_{zz} - I_{yy}) - \omega_z^2 I_{yz} - \omega_x\omega_z I_{xy} + \omega_y^2 I_{yz} + \omega_x\omega_y I_{xz} \qquad [8.5]$$

Because the diagonal elements enter as a difference, the contributions by the off-diagonal elements become relatively more significant. Also, the rotation rate around the z axis was about 100 times the average rotation rate around the x and y axes. For this reason we can ignore the last two terms in Equation 8.5, but have to account for the first three. Of these, the second varied relatively very little and was strongly correlated with a constant torque. Similar considerations for the other two axes led to the following equations:

$$\boldsymbol{\omega} \times \mathbf{I}\,\boldsymbol{\omega} \simeq \begin{pmatrix} \omega_y\omega_z(I_{zz} - I_{yy}) - \omega_x\omega_z I_{xy} \\ \omega_z\omega_x(I_{xx} - I_{zz}) + \omega_y\omega_z I_{xy} \\ \omega_x\omega_y(I_{yy} - I_{xx}) + \omega_x\omega_z I_{yz} + \omega_y\omega_z I_{xz} \end{pmatrix} \qquad [8.6]$$

where the first term in the equation for the z axis is fully defined by the first terms for the x and y axes. As this term is also, due its small size, badly determined, it was not solved for. In the implementations it was derived from the other calibrations and implemented as such. The complete calibration equations expressed in the observed quantities thus became:

$$\frac{\mathrm{d}\boldsymbol{\omega}}{\mathrm{d}t} = \begin{pmatrix} N_x/I_{xx} \\ N_y/I_{yy} \\ N_z/I_{zz} \end{pmatrix} + \begin{pmatrix} \omega_y\omega_z(I_{zz} - I_{yy})/I_{xx} - \omega_x\omega_z I_{xy}/I_{xx} \\ \omega_z\omega_x(I_{xx} - I_{zz})/I_{yy} + \omega_y\omega_z I_{xy}/I_{yy} \\ \omega_x\omega_z I_{yz}/I_{zz} + \omega_y\omega_z I_{xz}/I_{zz} \end{pmatrix} \qquad [8.7]$$

It is clear from this equation that only the ratios of the elements of the inertia tensor can be calibrated, not the absolute values. This was no problem, as similarly the application of the inertia tensor was primarily as ratios between the elements. In practice the elements were scaled to a fixed value for I_{xx} (see Table 7.1).

Calibrations were first carried out on data collected over one orbit at a time, for the inertia tensor elements and the external torques. The gravity gradient torque $\mathbf{N}_\mathrm{G}$ (see Section 7.2) was subtracted using an approximate *a priori* inertia tensor (correct to within a few per cent). Subsequently, the calibrations were repeated for the other external torques, applying the full, calibrated inertia tensor in Table 7.1:

$$\begin{pmatrix} N_x/I_{xx} \\ N_y/I_{yy} \\ N_z/I_{zz} \end{pmatrix} = \frac{\mathrm{d}\boldsymbol{\omega}}{\mathrm{d}t} + \begin{pmatrix} (\boldsymbol{\omega} \times \mathbf{I}\,\boldsymbol{\omega})_x/I_{xx} \\ (\boldsymbol{\omega} \times \mathbf{I}\,\boldsymbol{\omega})_y/I_{yy} \\ (\boldsymbol{\omega} \times \mathbf{I}\,\boldsymbol{\omega})_z/I_{zz} \end{pmatrix} - \begin{pmatrix} N_{\mathrm{G},x}/I_{xx} \\ N_{\mathrm{G},y}/I_{yy} \\ N_{\mathrm{G},z}/I_{zz} \end{pmatrix} \qquad [8.8]$$

where $\mathbf{N}_\mathrm{G}$ is given by Equation 7.6 in Section 7.2.

The coefficients which remained to be calibrated were those related to solar radiation and the magnetic moment of the satellite, as well as effects related to temporary localized heating of the outer surface of the satellite. Thus, the remaining torques were expressed as a set of harmonics, related to Equations 7.2, 7.4 and 7.5, and linked coefficients related to Equations 7.11 and 7.13. Some additional coefficients were required too, some possibly related to deformation of the Earth's magnetic field, others as yet unexplained.

Torques Related to Solar Radiation

Torques caused by solar radiation could be identified in three ways: they appeared as coefficients of specific trigonometric terms, related to the three-fold symmetry of the satellite (see Section 7.2), they disappeared during eclipses and sun-pointing mode observations, and they were subject to an annual variation resulting from the ellipticity

Table 8.4. The solar radiation related torque components as observed in the accelerations. The observed values, after having been corrected for Sun–Earth distance variations, were fitted to a linear function of time with day 800 as reference point. The coefficients (at day 800) are measured in mas s^{-2} and the derivatives in mas s^{-2} yr^{-1}.

Axis	Term	Coefficient	Derivative
x	$\sin\Omega$	−2.28005 ± 0.00031	−0.00980 ± 0.00042
x	$\sin 2\Omega$	0.59429 ± 0.00012	−0.00895 ± 0.00016
x	$\sin 4\Omega$	−0.20310 ± 0.00008	−0.00028 ± 0.00010
x	$\sin 5\Omega$	0.09826 ± 0.00008	−0.00230 ± 0.00011
x	$\sin 7\Omega$	−0.01112 ± 0.00009	0.00039 ± 0.00012
x	$\sin 8\Omega$	0.00375 ± 0.00009	−0.00025 ± 0.00012
x	$\sin 10\Omega$	0.01143 ± 0.00009	0.00218 ± 0.00012
x	$\sin 11\Omega$	0.00271 ± 0.00009	0.00074 ± 0.00012
y	$\cos\Omega$	−2.16908 ± 0.00024	0.01662 ± 0.00032
y	$\cos 2\Omega$	−0.64572 ± 0.00011	−0.00968 ± 0.00015
y	$\cos 4\Omega$	−0.17513 ± 0.00008	0.00319 ± 0.00011
y	$\cos 5\Omega$	−0.09407 ± 0.00010	−0.00099 ± 0.00013
y	$\cos 7\Omega$	0.00948 ± 0.00011	0.00152 ± 0.00014
y	$\cos 8\Omega$	−0.00562 ± 0.00010	0.00000 ± 0.00013
y	$\cos 10\Omega$	0.01117 ± 0.00009	0.00020 ± 0.00011
y	$\cos 11\Omega$	0.00205 ± 0.00008	0.00036 ± 0.00011
z	$\sin 3\Omega$	−0.77013 ± 0.00022	0.00261 ± 0.00029
z	$\sin 6\Omega$	−0.12250 ± 0.00008	0.00337 ± 0.00011
z	$\sin 9\Omega$	−0.02593 ± 0.00006	0.00049 ± 0.00008
z	$\sin 12\Omega$	−0.01035 ± 0.00006	0.00106 ± 0.00007

of the Earth's orbit. In fact, the torque variations may allow a measurement of the eccentricity value of the Earth's orbit to better than a few per cent.

Figure 8.11 shows the principal solar radiation torque related coefficients before correction for the varying distance to the Sun, Figure 8.12 shows the same after correction for this effect. There were drifts observed for most solar radiation related coefficients. These drifts can probably be explained as due to changes in the structure of the outer surface of the satellite due to exposure to radiation.

During periods of sun-pointing observations, the solar radiation torques virtually disappeared. With the z axis pointing towards the Sun, the radiation forces were almost completely balanced with respect to the centre of mass. The torques around the z axis were found to be more variable at times of long eclipses, possibly related to the cooling of the outer surface of the satellite during the eclipse, and the heating up during the perigee passage. The results for the solar radiation torques, normalised to a distance of 1 AU, are summarised in Table 8.4.

Calibration of Magnetic Moments

The magnetic moments around the satellite axes were calibrated in a simultaneous solution for the observations on all three axes, using Equation 7.13. The x component was, however, difficult to determine as it was for most of the orbit strongly correlated with other coefficients. Figure 8.13 shows the observed values for the magnetic moments

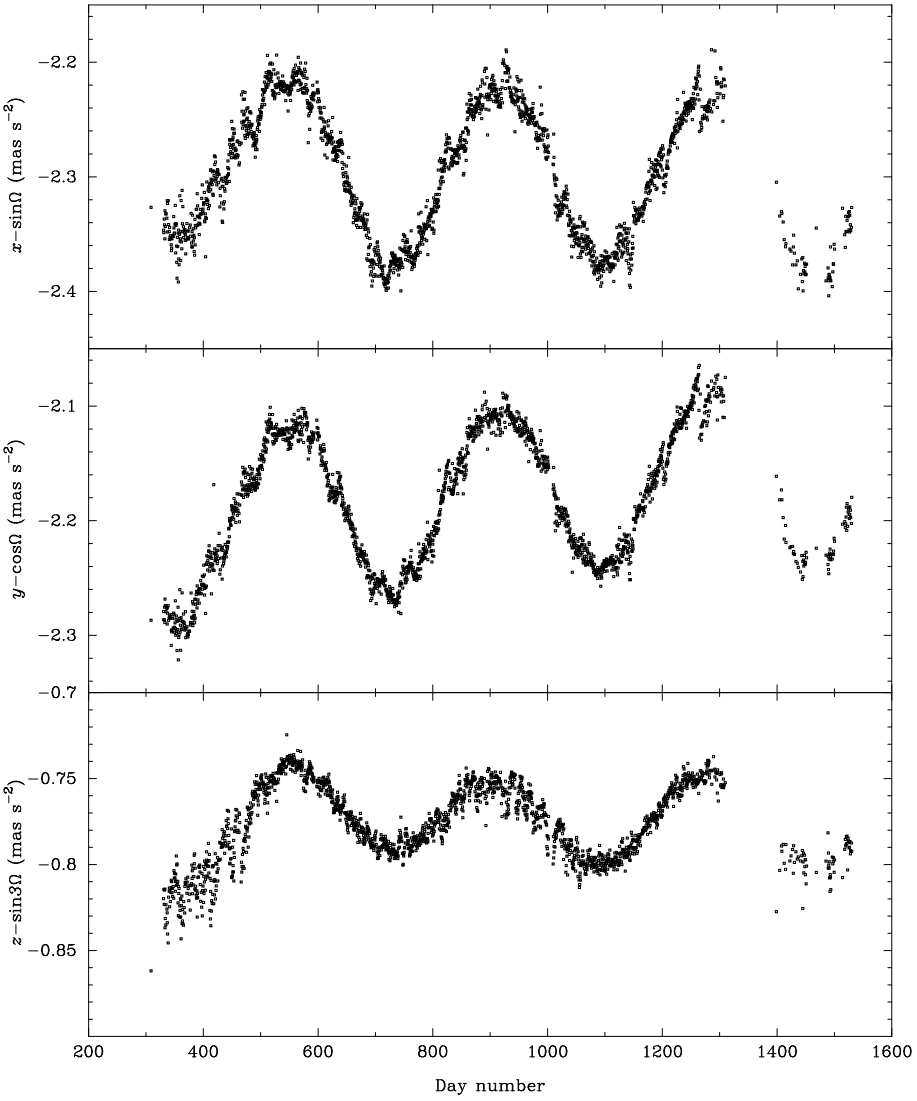

Figure 8.11. *The primary components of solar radiation torque observed in the accelerations around the three axes.*

over the mission. Magnetic moments were noticed clearly around the *y* and *z* axes, at a level of -2.7 Am^2 and $+0.3$ Am^2 respectively. The *y* axis component was very stable over the mission, the *z* axis component drifted slowly and showed more variation.

An additional *z* axis component, at -2.2 Am^2, was noted during eclipses. This component appeared to be related to the change in power supply from the solar panels to the batteries, although all cabling associated with the power supplies appeared to be properly shielded according to the design drawings. This component was given a fixed value if insufficient data covering an eclipse was available.

Remaining Coefficients

Four coefficients were used in the *z* axis torque representation that had no immediate explanation in terms of solar radiation: $\cos\Omega$, $\sin\Omega$, $\cos 2\Omega$ and $\sin 2\Omega$. The first two may be related to the Earth's magnetic field, but were not removed with a magnetic moment around the *x* and *y* axes. They may possibly represent a distortion of the

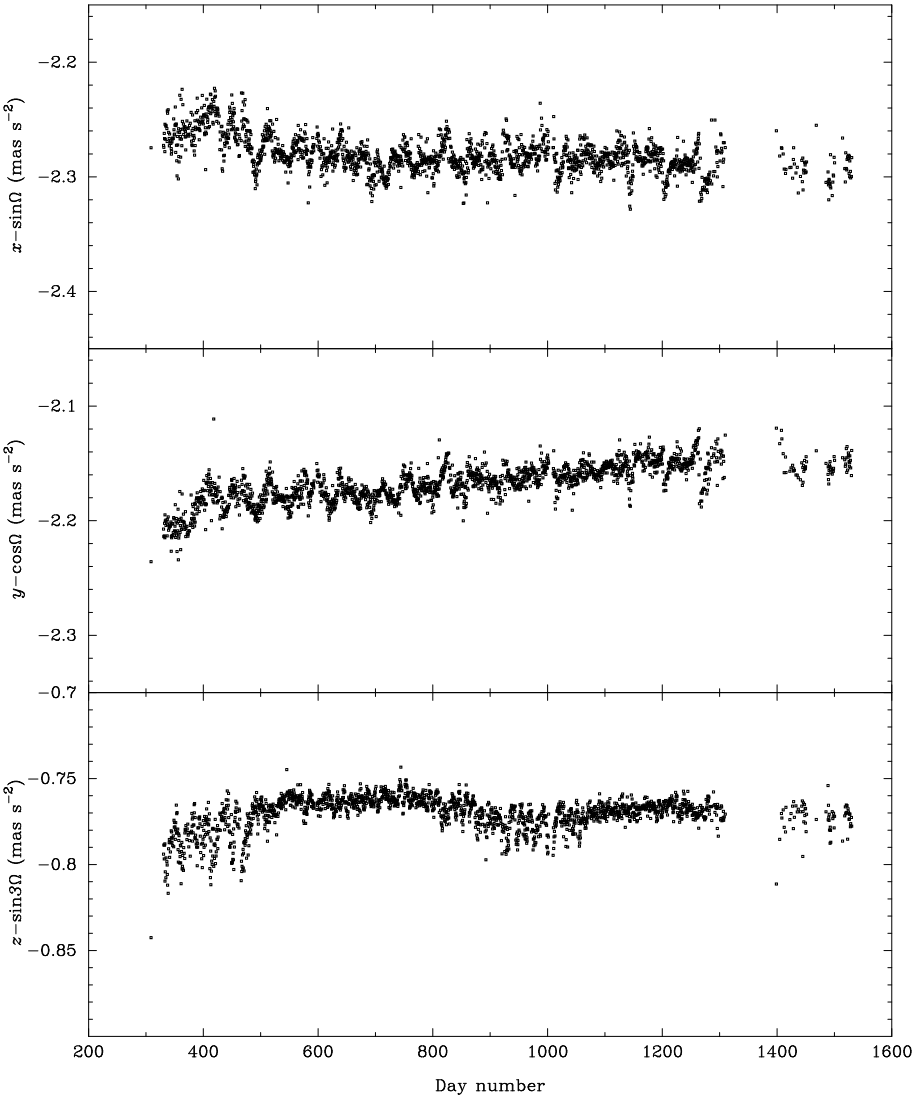

Figure 8.12. *As Figure 8.11, but corrected for the varying distance between the Earth and the Sun.*

magnetic field: their variation resembles the period of 57 days (the spin period of the rotation axis of the satellite) and the period of 588.7 days between two successive conjunctions between the Sun and the satellite at perigee. Another indication that these coefficients represent the magnetic field distortion comes from their correlation with variation on the constant in the *x* coordinate solution, which indicates that it could be the *y* axis magnetic moment that gives rise to these coefficients. Figure 8.14 shows these three coefficients.

The other two coefficients for the *z* axis are more difficult to explain. Their variability shows a semi-regular behaviour with a period of 28 days, half the spin period of the rotation axis of the satellite. This kind of behaviour would be expected from a gravity gradient related coefficient (see Equation 7.8). The $\sin 2\Omega$, however, is also likely to be related to the solar radiation torques, as seems to be indicated by the way it changed when the satellite went into sun-pointing mode. There is also a resemblance in behaviour between these two coefficients and the $\cos\Omega$ coefficient for the *x* axis.

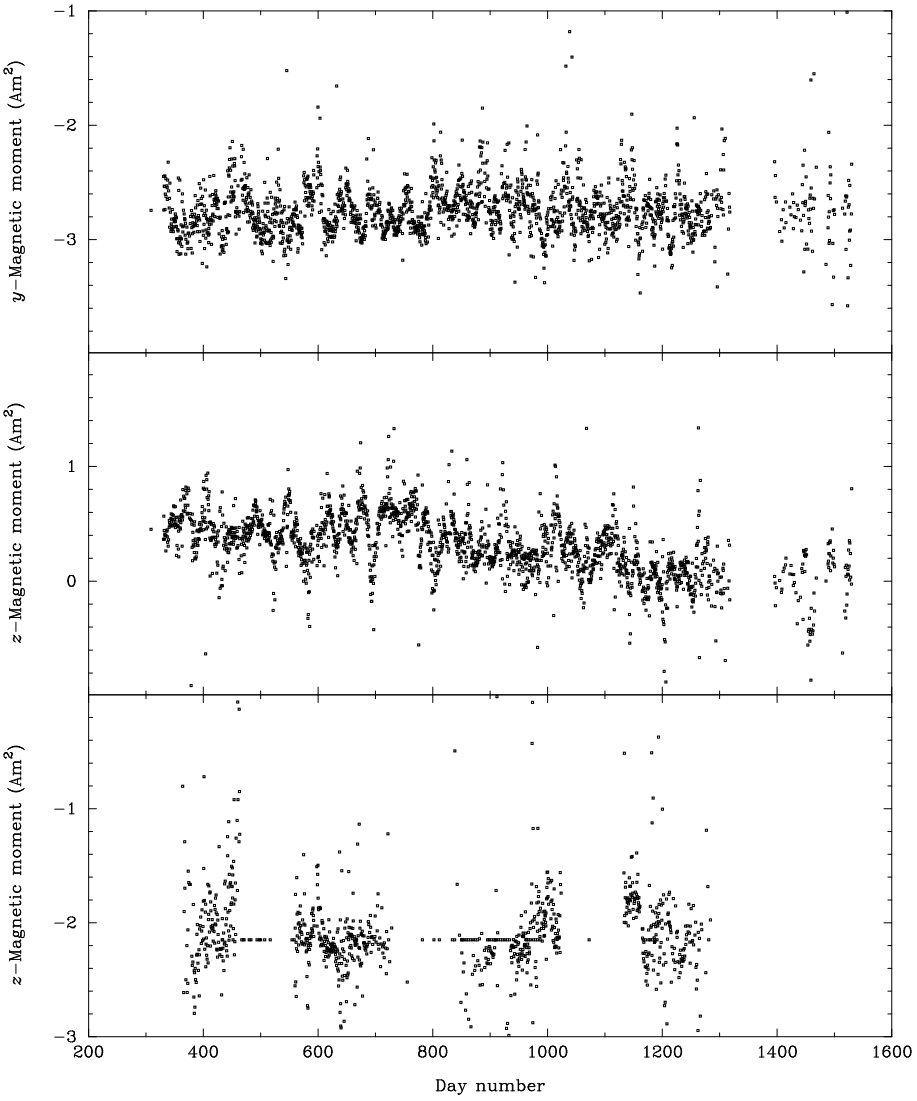

Figure 8.13. *The measurements of the magnetic moments of the satellite. The y-component is most clearly present. There is probably also a z-component during normal observing conditions (middle graph) and there appears to be a significant z-component during eclipse conditions (bottom graph). The eclipse related component could only be solved for under good conditions: converged attitude during most of an eclipse and at least two complete revolutions of the satellite outside the eclipse.*

The constant for the *y* axis (Figure 8.15) showed a long-term exponential decrease, a 57 day modulation with varying amplitude, and short-term variations explained below. The exponential decrease was probably related to changes in the outer surface of the satellite due to exposure to solar radiation. The exact zero point for this term is badly determined as it depends strongly on the value used for the component I_{yz} of the inertia tensor (see Equation 8.5). The modulation is probably related to a magnetic moment on the *x* axis, although entering this as a degree of freedom in the solutions did not give a consistent result (partly due to correlations with other coefficients). The points near days 1000, 1300 and 1450, which are offset by about 0.2 mas s^{-2}, are related to sun-pointing mode observations. Their offset indicates that the constant on the *y* axis could be solar radiation related, and representing a spinning motion driven by an insufficiently balanced torque around the *y* axis. The gap around day 750 is due to the running of

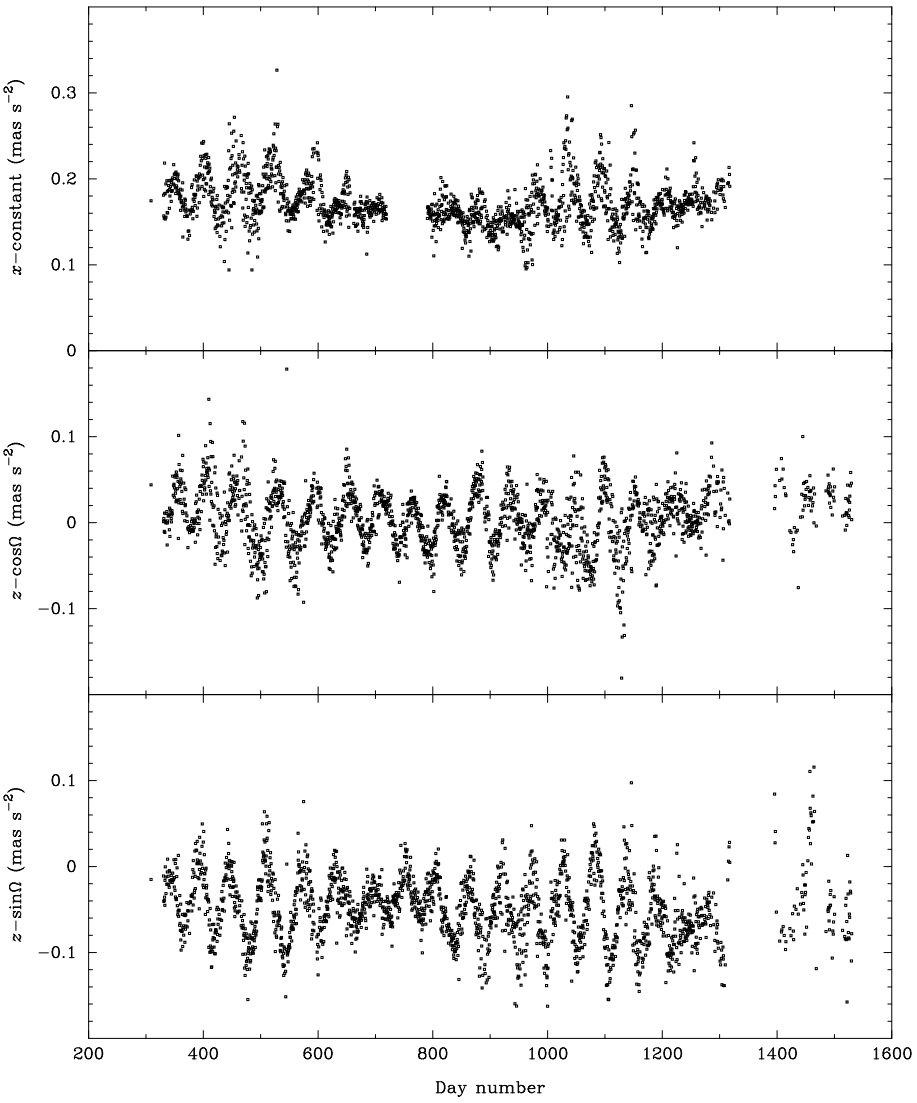

Figure 8.14. *Three coefficients, showing through their variability a possible link with the magnetic moment of the satellite and a distortion of the Earth's magnetic field at high altitudes. The short-period variation is probably related to the spin period of the satellite z axis (57 days). The long-period modulation appears to be related to the period between two conjunctions of the Sun and the satellite at apogee (588.7 days).*

gyro 4 in addition to gyros 1, 2 and 5. This caused additional torques on the *x* and *y* axes (see Section 8.6).

A number of coefficients show short-term variations with correlations between alternate orbits, in particular when the perigee of the satellite orbit was low. The longitude of alternate orbits changed by only 40°; between successive orbits the change was 160°. Thus, the conditions around a perigee passage for alternate orbits were likely to be more similar than between successive orbits, in particular concerning the results of friction by the outer layers of the atmosphere. One of the finest examples is shown in Figure 8.16 for the constant torque on the *y* axis. A constant torque either originated in the spacecraft (gyro-induced) or represented a local (on the spacecraft) external and unbalanced torque. It appears that the satellite was heated up on one side during a perigee passage, with the amount of heating depending on the conditions of the outer

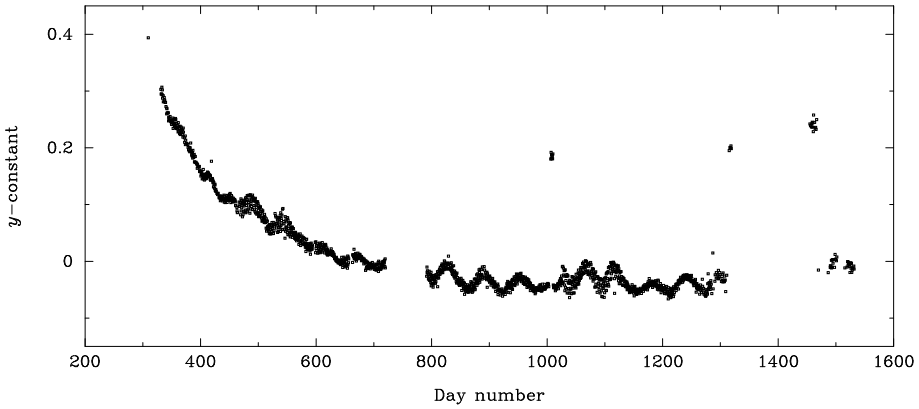

Figure 8.15. *Long-term variations in the constant for the y coordinate, showing a kind of exponential decrease as well as a 57 day modulation.*

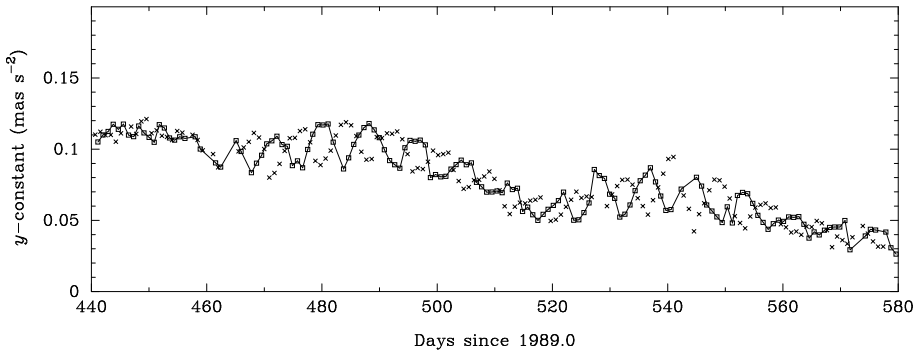

Figure 8.16. *Short-term variations in the constant for the y coordinate, showing the effect of alternating local longitudes of the perigee during a period with very low perigee height. Orbits with even numbers are indicated with a cross, odd-numbered orbits with an open square, and have been connected to show their correlation.*

atmosphere of the Earth and therefore being correlated between alternate orbits. During the orbit following the perigee passage the local heat loss from the satellite produced the windmill effect.

8.6. Miscellaneous Effects

The remaining effects were of short, or even impulse, nature. They concerned hits of the satellite by external objects (two fairly major ones, causing rotation rate changes of the order of 2 arcsec s^{-1}, and 10 to 15 smaller ones); gyro de-storage, causing temporary torques during spin-up and spin-down procedures, and, during operations of the additional gyro, an offset in the constant related to the inertia tensor, the spinning rate of the satellite and the angular momentum of the additional gyro. In the case of gyro 4, the offsets observed were 2.200 mas s^{-2} in the x coordinate, and 3.305 mas s^{-2} in the y coordinate. Using the inertia tensor values given in Table 7.1, this gives values of -5.70 μNm and -9.45 μNm for the nominal induced torque of gyro 4, compared to the values given in Table 7.2: -5.52 μNm and -9.01 μNm, indicating that the orientation

of the rotation axis was correctly recovered, but that the angular momentum of gyro 4 appeared to be 4 per cent higher than expected (unless the much less likely possibility that the entire inertia tensor is 4 per cent too low).

The final source of disturbances came from the reaction of the solar-panel hinges on the temperature changes when the satellite moved into an eclipse. These were noticeable only in the great-circle reduction, described in the next chapter, and caused a small saw-tooth like behaviour of the spin-phase.

8.7. Conclusions

The calibration results presented above show some of the problems encountered when trying to operate satellites with very high pointing accuracy in one-axis-stabilised mode. In the case of Hipparcos these problems were largely aggravated by the orbital conditions, but the same orbital conditions allowed the recognition of some contributions (in particular the magnetic moment) that would otherwise have been difficult to observe. Important improvements in the torque modelling would probably be obtained with the full implementation of the correct inertia tensor and a description of the deformation of the Earth's magnetic field (for which some models are available). In addition, torques as produced by the gyros were not strictly smooth, but rather like a semi-regular string of small impulses and it still needs to be investigated to what precision the current approximation as smooth torques was valid.

F. van Leeuwen